

Effect of Cationic Interface Defects on Band Alignment and Contact Resistance in Metal/Oxide Heterojunctions

Michael Andrä,* Carsten Funck, Nicolas Raab, Marc-André Rose, Mykhailo Vorokhta, Filip Dvořák, Břetislav Šmíd, Vladimír Matolín, David N. Mueller, Regina Dittmann, Rainer Waser, Stephan Menzel, and Felix Gunkel*

Heterojunctions between high-work-function metals and metal oxides typically lead to Schottky-type transport barriers resulting from charge transfer between the neighboring materials. These yield versatile electronic functionality exploited for current rectification, memristive behavior, or photocatalysis. Height, width, and shape of the interfacial transport barrier are strongly affected by charge screening via ionic defects, which are often extremely difficult to probe. The ionic nature of a variable contact resistance in heterojunctions between Nb-doped SrTiO₃ (Nb:SrTiO₃) and platinum is explored. A control of cationic vacancy defects at the interface is achieved by different annealing procedures in oxidizing and reducing conditions before establishing Pt/Nb:SrTiO₃ heterojunctions. Detailed analysis of electronic transport across the heterojunctions reveal significantly varied transport barriers resulting from the cationic defect structure at the interface. These findings are supported by conductive-tip atomic force microscopy and in situ photoemission spectroscopy showing diminished conductivity of the Nb:SrTiO₃ surface and the formation of an insulating surface skin layer after oxygenation. At high doping level, oxygen stoichiometry cannot explain the observed behavior. The increased transport barrier height is therefore linked to strontium vacancy defects. The tailored cation disorder yields access to the ionic control of electronic transport in functional oxide heterojunctions.


has therefore become one of the most important strides in oxide electronics,^[6,7] but also in the design of epitaxial Li-ion batteries^[8–11] and water splitting catalysts.^[12–14] A prototype—and supposedly simple—case is the heterojunction of a transition metal oxide with a high work function metal such as Pt, forming Schottky-type transport barriers, which promote diode-like device characteristics, functional in electronic^[1–4,15–21] and photonic concepts.^[22–25]

While Schottky-type transport barriers typically result from electronic charge transfer from the metal-oxide to the metal, complex oxides also offer a wide variety of mobile ionic defects. These provide additional ionic charges that affect the electronic charge screening within the Schottky contact.^[17,26,27] The Pt/Nb:SrTiO₃ heterojunction is a prominent example, as its interfacial contact resistance results in a (fairly simple) metal–insulator–metal (MIM) structure, possessing rectifying *I*(*V*)-characteristics, memristive switching behavior,^[1,4,5,17,28] photo-catalytic activity^[22]

and sensor characteristics.^[29,30] These properties are highly sensitive to the ionic constitution of the heterojunction's interface. To this end, the resistance switching behavior of these junctions can be attributed primarily to oxygen (vacancy)

Metal/metal-oxide heterojunctions are essential building blocks in state-of-the-art oxide electronics. They represent lead contacts to external voltage supply, but also potential devices themselves.^[1–5] Active engineering of heterojunction interfaces

M. Andrä, Dr. N. Raab, Prof. R. Dittmann, Prof. R. Waser, Dr. S. Menzel, Dr. F. Gunkel
 Peter Grünberg Institute 7
 Forschungszentrum Juelich GmbH, and Juelich-Aachen Research
 Alliance for Fundamentals on Future Information Technology (JARA-FIT)
 52425 Juelich, Germany
 E-mail: m.andrae@fz-juelich.de; f.gunkel@fz-juelich.de

 The ORCID identification number(s) for the author(s) of this article can be found under <https://doi.org/10.1002/aelm.201900808>.

© 2019 The Authors. Published by WILEY-VCH Verlag GmbH & Co. KGaA, Weinheim. This is an open access article under the terms of the Creative Commons Attribution License, which permits use, distribution and reproduction in any medium, provided the original work is properly cited.

DOI: 10.1002/aelm.201900808

C. Funck, M.-A. Rose, Prof. R. Waser, Dr. F. Gunkel
 Institute of Electronic Materials (IWE2)
 RWTH Aachen University and JARA-FIT
 52074 Aachen, Germany

Dr. M. Vorokhta, Dr. F. Dvořák, Dr. B. Šmíd, Prof. V. Matolín
 Department of Surface and Plasma Science
 Faculty of Mathematics and Physics
 Charles University
 V Holesovickach 2
 180 00 Prague, Czech Republic

Dr. D. N. Mueller
 Peter Grünberg Institute 6
 Forschungszentrum Juelich GmbH, and Juelich-Aachen Research
 Alliance for Fundamentals on Future Information Technology (JARA-FIT)
 52425 Juelich, Germany

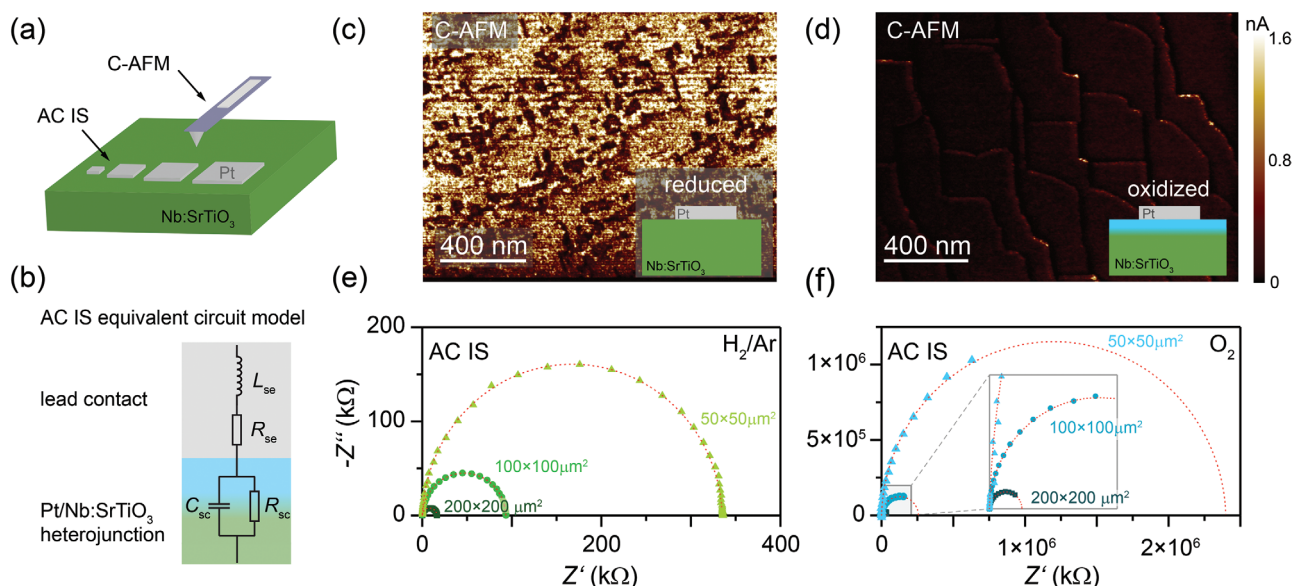


Figure 1. a) Schematic illustration of the sample stack used for the AC impedance spectroscopy (AC IS) experiments and the $I(V)$ -curves; b) the equivalent circuit model used for the fitting of the IS data. (c,d) illustrate conductive-tip atomic force microscopy measurements on n -SrTiO₃ single crystals after *in-situ* annealing in oxidizing and reducing conditions. (e,f) show impedance spectroscopy data after annealing in H₂/Ar and in O₂ gas atmospheres for different Pt pad sizes (50 × 50 μm² up to 200 × 200 μm²). The dashed lines indicate data fits.

chemistry. High and low resistance states of the device are realized by a redistribution of oxygen vacancy defects within the Schottky contact.^[3,15,31,32] Most studies across the literature therefore limit their discussion of ionic defects to oxygen vacancy defects, while other types of ionic defect species are often ignored. Thermodynamically, however, the defect structure of Nb:SrTiO₃^[26,33] and in particular of its surface^[29,30,34] involves additional defect formation processes, which become particularly important at high dopant concentration and go beyond standard oxygen chemistry: Upon oxidation, the redox-chemistry of Nb:SrTiO₃ forces the formation of negatively charged strontium vacancies^[27,30,34,35] as a natural result of Schottky disorder.^[33,36,37] Cation vacancy defects are acceptor-type defects, counter-compensating the extrinsic donor doping and lowering the electron concentration in the material.^[33,34,36,37] In the near-surface region, where ionic defect dynamics differ significantly from the bulk, the Schottky defect-equilibrium has been found to be active at temperatures as low as 670 K,^[29,30] making it relevant for almost any thermal treatment of Nb:SrTiO₃ single crystals or thin films. For bare Nb:SrTiO₃ surfaces, the formation of cationic surface defects results in an insulating skin layer forming during oxidation^[33,34,37] and leading to poor surface conductivity even in highly n -doped compounds. For Pt/Nb:SrTiO₃ heterojunctions, strontium vacancy defects likewise reflect localized negative charges located at the interface, that (if present in sufficient concentration) enhance the effect of electron depletion at the interfacial Schottky contact. Strontium vacancy defects hence represent intrinsic means to tailor the charge screening at the interface, and thus height and width of the transport barrier established in the initial state of the junction.

In this study, we demonstrate varied transport barriers through control of the intrinsic cation defect chemistry, realized by different pre-annealing procedures applied to

Nb:SrTiO₃ single crystals before heterojunction fabrication. The link between electronic properties of the heterojunction and cationic interface defects is inferred from *in situ* spectroscopy and density functional theory, revealing an enhanced transport barrier in presence of cationic vacancy disorder. As we discuss, engineering this cationic disorder in complex oxides allows to tailor interfacial band alignment as well as the resulting transport characteristic in metal/metal-oxide heterojunctions. Based on fundamental thermodynamics of Schottky-disorder,^[36] this procedure may be generalized to most n -type oxides explored today.

In **Figure 1**, we analyze the AC impedance spectroscopy (AC-IS) response of Pt/Nb:SrTiO₃ heterojunctions. The heterojunctions were obtained on Nb:SrTiO₃ single crystals that—prior to Pt deposition—underwent preannealing procedures (24 h/1050 – 1150 °C) in O₂ and in Ar/H₂ gas mixture, respectively. Micrometer devices with pad sizes between 50 × 50 μm² and 200 × 200 μm² were investigated (Figure 1a). All spectra (Figure 1e,f) consistently revealed a single semi-circle in the Cole–Cole diagram for all tested electrode areas and preannealing procedures, indicating a single parallel RC element in the circuit attributed to the Pt/Nb:SrTiO₃ heterojunction's Schottky-type transport barrier. The barrier results in an electron depletion layer associated with a finite capacitance (C_{sc}) and resistance (R_{sc}). All semi-circles were found to be offset along the real axis, indicating a finite series resistance ($R_{se} \approx 20 \Omega$) owing to the contact leads of the experimental setup, and could be approximated by the single RC-element equivalent circuit model (Figure 1b; corresponding Bode plots are shown in the Supporting Information).

After the annealing procedure in 4% H₂/Ar, AC IS reveals a substantial contact resistance $R_{sc} \approx 23 \text{ k}\Omega$ (330 k Ω) at a pad size of 200 × 200 μm² (50 × 50 μm²), characterizing the Schottky contact formed at the interface (Figure 1e). Remarkably, however,

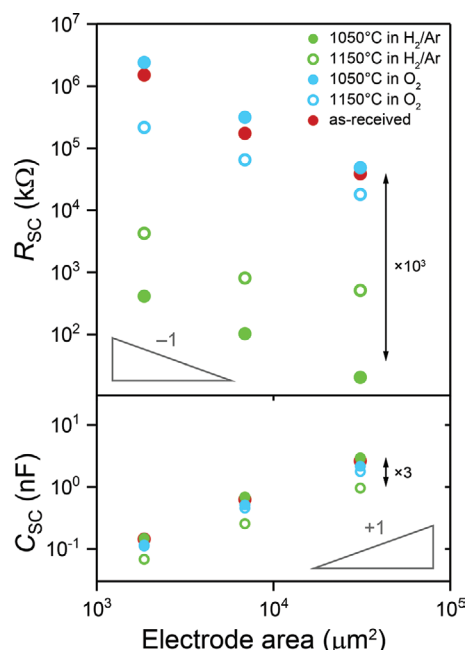


Figure 2. Contact resistance (R_{sc}) and capacitance (C_{sc}) as a function of Pt electrode size, as determined from impedance spectroscopy measurements on n -SrTiO₃ single crystals after different reducing and oxidizing annealing treatments. The red data indicates reference data obtained for a substrate as-received from the supplier, without any further treatment before Pt-electrode evaporation.

R_{sc} increases by three orders of magnitude to $R_{sc} \approx 39 \text{ M}\Omega$ ($200 \times 200 \mu\text{m}^2$) and even into the $\text{G}\Omega$ -regime ($50 \times 50 \mu\text{m}^2$) after annealing in oxygen (Figure 1f). The electronic properties of the Pt/Nb:SrTiO₃ heterojunctions have thus changed dramatically upon annealing. This finding is further corroborated by conductive-tip atomic force microscopy (C-AFM) measurements on the bare Nb:SrTiO₃ single crystal surfaces as shown in Figure 1c,d. After reduction (Figure 1c), the average current ($I \approx 1.5 \text{ nA}$) from the tip through the surface into the sample is significantly higher than after the oxidation process ($I \leq 500 \text{ pA}$, Figure 1d),

while the applied voltage was kept similar. (Note, that for comparison the C-AFM images were plotted on identical current scales to illustrate the conductivity contrast.) Hence, the surface resistance of single crystals annealed in more reducing environment is lower than the one observed for oxidized single crystals, indicating that the altered interface resistance observed in the impedance experiment results from an altered chemistry on the Nb:SrTiO₃ side of the heterojunction.

Figure 2 shows the electrode area-dependence of C_{sc} (bottom panel) and R_{sc} (top panel) determined from the impedance spectra. On double-logarithmic scales, both $C_{sc} (\propto A)$ and $R_{sc} (\propto 1/A)$ show a linear dependence on the top electrode area, indicating homogeneous interface properties over micrometer length scale.^[38] C_{sc} does not change significantly depending on the annealing treatment (within a factor of 3). Using classical plate capacitor physics, this corresponds to an almost constant effective barrier width in the range of $d_{sc} \approx 10\text{--}20 \text{ nm}$, that neither changes substantially upon annealing at varied temperature nor at varied oxygen atmosphere. For this estimate, we assumed a field-reduced effective dielectric constant of $\epsilon \sim 100$.^[39,40] In contrast to the interface capacitance, R_{sc} does depend significantly on the presence of oxygen during annealing. Consistently for all electrode areas, R_{sc} is found approximately three orders of magnitude lower after annealing in H₂/Ar gas mixture than after annealing in oxidizing conditions. Together, these findings point toward changes in the transport barrier height at comparably similar barrier width.

Figure 3 shows $I(V)$ -curves measured in forward direction (positive potential) for different electrode areas after annealing in H₂/Ar gas mixture (a) and in oxidizing conditions (b), with linear (logarithmic) current-scale in the top (bottom) panels. The $I(V)$ -curves show a strongly non-linear behavior consistent with the non-Ohmic contact resistance, whereas heterojunctions obtained after annealing in H₂/Ar gas mixture deliver considerably higher currents as compared to the ones obtained after oxygenation of the Nb:SrTiO₃ single crystals, consistent with the C-AFM measurements shown in Figure 1c,d.

At an applied voltage of 450 mV, the currents are still largely suppressed by the diode characteristics of the heterojunction

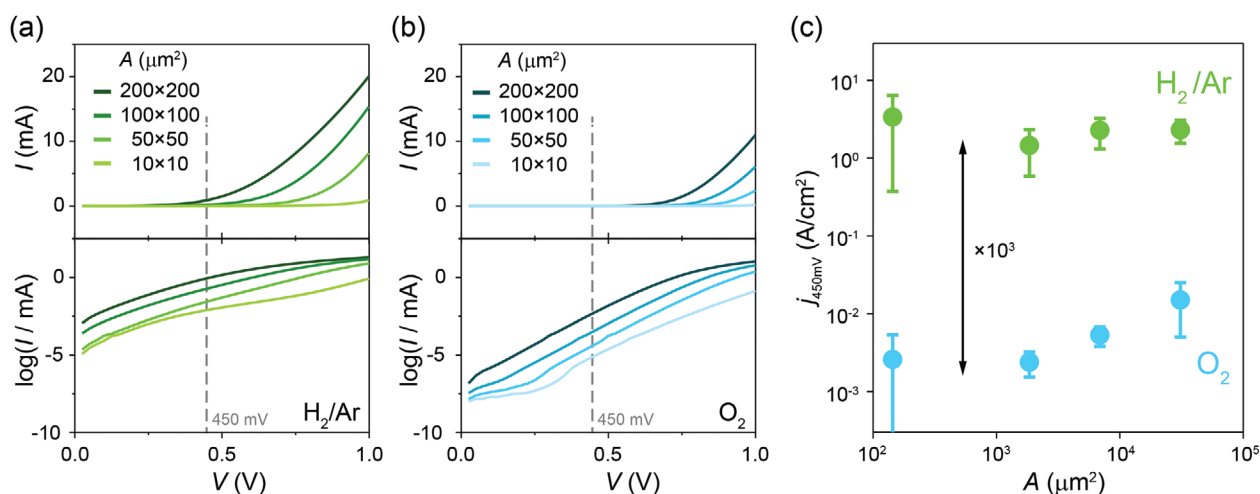


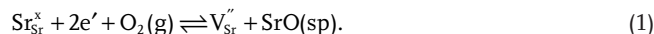
Figure 3. Electrode area-dependent $I(V)$ -curves measured on n -SrTiO₃/platinum contacts after reducing (a) and oxidizing (b) annealing and the corresponding current densities determined at 450 mV (c).

as the transport barrier is not exceeded. Therefore, the current density at this potential is a measure of the actual barrier height. As illustrated in Figure 3c, heterojunctions realized on oxidized single crystals provide 2–3 orders of magnitude lower current density than the ones realized on reduced single crystals, indicating an increased barrier height formed at heterojunctions to Nb:SrTiO₃ after oxygenation. (Note that a direct determination of the Schottky barrier height from $I(V)$ -characteristics is only valid for a strict transport mechanism for electrons over the barrier. As a detailed analysis of $I(V)$ -curves across similar heterojunctions have revealed considerable tunneling contributions through the barrier,^[41,42] we refrain from such analysis and limit our discussion here to the comparison of absolute current densities.)

In order to understand the observed modifications of the transport barrier in detail, we consider the defect chemistry of Nb:SrTiO₃ and discuss the different chemical constitutions expected for its surface after the different annealing procedures. Oxygen vacancies are obvious candidates of ionic defects that may be present in different quantities after annealing in reducing and oxidizing conditions. In order to have a significant impact on charge screening in the heterojunction, however, their concentration must exceed the extrinsic donor concentration of $1.5 \times 10^{20} \text{ cm}^{-3}$. Thermodynamically, it is extremely difficult to incorporate such high concentrations of oxygen vacancies in SrTiO₃, even at elevated temperatures and heavily reducing gas atmospheres (H₂/Ar gas mixture provides oxygen pressures in the range of $10^{-13} < p_{\text{O}_2}/\text{Pa} < 10^{-10}$ at temperatures of 1050–1150 °C). The thermodynamic equilibrium concentration of oxygen vacancies under such conditions can be estimated from bulk defect chemistry models (see e.g., refs. [26,33,34,43]) and does typically not exceed the order of 10^{19} cm^{-3} .^[44,45] Also surface accumulation of oxygen vacancies in SrTiO₃ typically remains below a concentration of 10^{20} cm^{-3} , when generated through thermodynamic treatments.^[43,46,47]

Consistent with this, for all treated single crystals the electron concentrations determined by in-plane Hall measurements coincided with the Nb concentration indicating that the oxygen vacancy content in the bulk of all samples is significantly below the extrinsic dopant concentration. Therefore, oxygen vacancies can be considered less important for charge screening in the heterojunctions obtained after thermodynamic annealing.

Certainly, higher oxygen vacancy concentrations are accessible in non-equilibrium processes such as the resistive switching of SrTiO₃^[16,31] or X-ray irradiation-induced defect formation,^[48–50] thus playing a key role in those cases. Here, however, we consider intrinsic cationic disorder thermodynamically induced in Nb:SrTiO₃ via Schottky disorder, which becomes the dominant defect formation mechanism in *n*-type oxides upon oxygenation.^[34,36,51] For SrTiO₃, Schottky-disorder primarily takes place by the formation of negatively charged strontium vacancy defects (V_{Sr}'') and precipitation of strontium oxide (SrO(sp)), as described by the partial Schottky reaction



This process starts from the surface of SrTiO₃ and evolves over time via diffusion into the bulk.^[29,30,34,52] The formation of Sr vacancy defects manifests itself by a shift of the Fermi-level into the band gap, as the sample is oxidized.^[29] Figure 4 illustrates valence band (VB) spectra obtained on the bare surface of Nb:SrTiO₃ by in situ x-ray photoemission spectroscopy (XPS) at elevated temperature of 670 K and under applied oxygen atmosphere (near ambient pressure (NAP) XPS). A shift of all VB spectra toward lower binding energies (E_{B}) is observed as the ambient oxygen pressure is increased (Figure 4a), indicating a shift of the Fermi level from the conduction band edge into the band gap ($E_{\text{gap}} \sim 3 \text{ eV}$).^[33] Note that all core level spectra show a similar and rigid shift as discussed in ref. [29] and as illustrated in the Supporting Information. Figure 4c shows the position

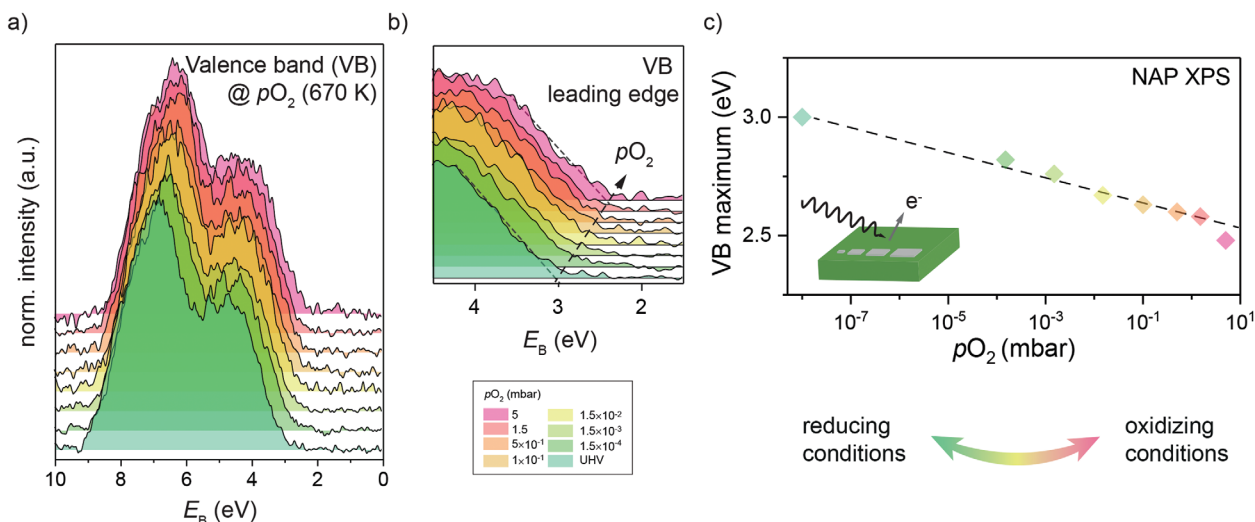


Figure 4. Valence band spectra taken by in situ photoemission spectroscopy in controlled oxygen atmosphere. a) shows the entire VB region, while b) enlarges the view on the VB tailing edge. The dashed lines are guides-to-the-eye illustrating the energy shift of the valence band maximum (VBM), plotted as a function of applied oxygen pressure in c) [Error bars resulting from the fit of the intercept are about $\pm 50 \text{ meV}$]. A significant shift of the spectra toward lower binding energies is observed as more and more oxygen is applied, as a result of Sr vacancy formation at the surface of Nb:SrTiO₃. (Corresponding core level spectra of Ti 2p, Sr 3d, and O 1s are illustrated in the supplementary information file.)

of the VB maximum (VBM) as a function of ambient oxygen pressure ($p\text{O}_2$), approximated from the intercept of a linear fit to the VB trailing edge (Figure 4b). The shift of the Fermi level from the conduction band edge (as observed in reducing conditions/UHV) into the band gap indicates electrons are increasingly depleted from the surface upon oxygenation, resulting in an insulating surface skin layer.^[29,30,53] The absolute positions of the VBM furthermore indicate effective underdoping of the Nb:SrTiO₃ surface in oxidizing conditions, that is, an effective donor-concentration which is lower than expected from the extrinsic Nb-concentration. In turn, this excludes a scenario of *overdoping*, that is, an effective donor doping through oxygen vacancies, when reducing conditions are applied. In the near-surface region, Nb-dopants (keeping the Fermi level close to the conduction band) are hence counter-compensated through ionic Sr vacancy defects as the sample gets oxidized. This process is concomitant with subtle changes in the Sr core level spectra, which are not resolved in standard lab-based XPS, but evident in more-surface sensitive, synchrotron-based NAP-XPS analysis.^[30]

To explore in more detail whether the effect of Sr vacancy formation is also responsible for the modification of the Schottky barrier observed in the Pt/Nb:SrTiO₃ heterojunctions, we employ quantum mechanical simulations based on density functional theory combined with the non-equilibrium Green's function formalism (DFT + NEGF), that provide the local density of states (LDOS) across the heterojunction.^[41,42] Two atomic configurations were investigated: one pristine heterojunction without any distortion of the lattice and one with a distortion by a Sr vacancy defect (equivalent to a volume concentration of 2.2 at% in the $2 \times 2 \times 11$ supercell), reflecting the ionic constitution of Nb:SrTiO₃ treated under reducing and oxidizing conditions, respectively. The red circle in Figure 5a marks the strontium atom that was removed for the calculation, the blue circles indicate the positions of the Nb dopants.

From DFT + NEGF, the position of the conduction band and the valence band as well as their band bending towards the Schottky interface was extracted.^[54] Figure 5b,c show the calculated LDOS without and with a Sr vacancy defect, respectively, plotted as a function of position (d) across the heterojunction. Purple color indicates regimes of large LDOS while black color indicates regimes of low LDOS. For the platinum electrode ($4\text{ nm} \lesssim d \lesssim 6\text{ nm}$), we determined a high density of electronic states at the Fermi level (ϵ_F) as expected for the metal. On the Nb:SrTiO₃ side of the heterojunction ($0\text{ nm} \lesssim d \lesssim 4\text{ nm}$), the black regime describes the band gap between valence band and conduction band of SrTiO₃. Due to the Nb-doping, ϵ_F is located in the conduction band, as one moves away from the heterojunction's interface ($d = 0$). In the central Schottky contact region ($1\text{ nm} \lesssim d \lesssim 4\text{ nm}$) the concentration of electronic states at the Fermi level vanishes, as the conduction band moves up in energy representing the Schottky-type electron depletion region at the interface. As a result, ϵ_F moves deeper into the band gap forming the barrier for electron transport through the junction.

Figure 5b describes the pristine *n*-type Schottky barrier formation in the undistorted case. The resulting Schottky barrier height ($e\phi_{\text{SBH}}$) is 1.2 eV. Introducing a strontium vacancy defect near the interface, $e\phi_{\text{SBH}}$ significantly increases by 0.3 eV to a total barrier height of 1.5 eV (Figure 5c). In addition, the shape

of the barrier is slightly broadened, which is consistent with the presence of the additional negative charge of the strontium vacancy defect within the heterojunction. Both results, a significant increase of the barrier height and a slight broadening of the space charge layer, are observed independent of the actual positions chosen for the Sr vacancy defect (the detailed shape of the barrier may change upon a variation of the defect location).

All results obtained experimentally showed a dependence of the interfacial transport barrier in Pt/Nb:SrTiO₃ heterojunctions on the pre-treatment procedure applied to Nb:SrTiO₃ before heterojunction fabrication. After oxidation, impedance spectroscopy and $I(V)$ -curves consistently showed a significantly increased R_{sc} due to enhanced carrier depletion at the interface, while the width of barrier as indicated by C_{sc} did not change substantially. Wang et al. previously showed that regardless of the transport mechanism through the barrier (direct tunneling, Fowler-Nordheim tunneling, thermionic emission, hopping conduction) R_{sc} depends exponentially on the transport barrier height.^[55] Hence, a 0.3 eV-change in barrier height would change the contact resistance by a factor of $\exp\left(\frac{e\Delta\phi_{\text{SBH}}}{k_{\text{B}}T}\right) \approx 10^5$.

This can easily explain the changes in contact resistance observed in the impedance experiment as well as in $I(V)$ -characterization, which revealed a 2–3 orders of magnitude change (Figure 3). The remaining over-estimation obtained from DFT is a result of the high concentration of donors (about 6.8 at%) and Sr vacancy defects (2.2 at%) assumed in the calculation in order to limit the cell size and thus computational costs. In addition, the particular form of the barrier will depend on the exact positions of dopants and defects, locally resulting in higher/lower barriers, which is averaged in macroscopic measurements such as AC-IS or $I(V)$ -curves. C_{sc} depends inversely proportional on the barrier width, converting into a much weaker square-root-dependence on the barrier height,

$$C_{\text{sc}} = \epsilon_0 \epsilon_r \frac{A}{d_{\text{sc}}} \propto \frac{1}{\sqrt{\phi_{\text{SBH}}}}. \quad (2)$$

Here, ϵ_0 denotes the vacuum permittivity, ϵ_r the relative permittivity, and A the contact area. As an estimate, the calculated barrier heights translate into a relative change in capacitance by a factor of $\sqrt{1.5/1.2} \approx 1.1$, appearing as an unchanged value given the general scatter of the data shown in Figure 2. (Note that the absolute screening length revealed from DFT is shorter than the one determined in experiment, which is again due to the larger dopant concentrations applied in the theory approach.)

Based on classical defect chemistry in combination with DFT calculations we therefore argue that the formation of strontium vacancy defects at the surface of Nb:SrTiO₃ during oxidation is responsible for the observed behavior. The incorporation of Sr vacancy defects into Nb:SrTiO₃ surfaces in oxidizing conditions—based on fundamental thermodynamics of Schottky disorder—is a well-reported,^[33,34,36] yet less well-considered process. As we show, however, the presence of localized negative charges associated with cationic disorder can be used to tailor barrier heights in Pt/Nb:SrTiO₃ heterojunctions. For the functionality of such devices, this translates into the opportunity to tailor band alignments by the control

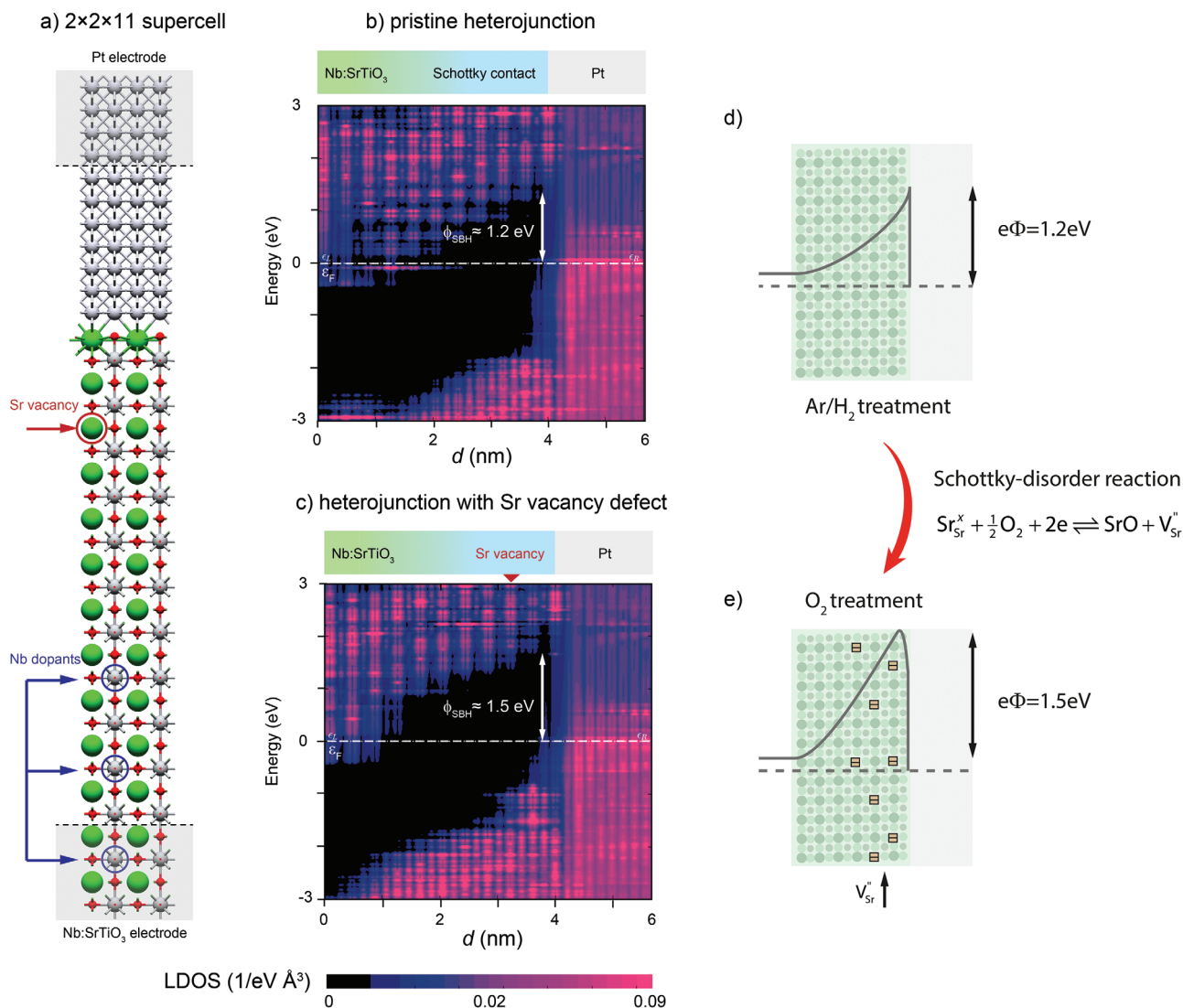


Figure 5. DFT + NEGF simulations of Pt/Nb:SrTiO₃ heterojunctions. The atomic model is shown in (a). The local density of states is plotted for calculations without (b) and with (c) a strontium vacancy in the near contact region. The purple regime indicates a high concentration of electronic states while the black regime indicates a low concentration of electronic states.

of intrinsic cationic disorder,^[28,56] to produce heterojunctions with strongly rectifying behavior or with more symmetric $I(V)$ -characteristics, or to affect their photocatalytic response.^[22] As for resistive switching devices, the initial state of the device could be varied, but also the subsequent cycling of the cells, where the redistribution of oxygen vacancies into the depletion region at the heterojunction is responsible for the resistive switching effect.^[4,17,57,58]

Cationic disorder leads to a finite concentration of ionic (trap) charges, that influence band bending, contact resistances, and all related physical properties of the heterojunction. Given that most Nb:SrTiO₃ single crystals are typically annealed in oxygen atmospheres prior to application (also including single crystalline substrates for thin film growth), the presence of cationic defects at surfaces and interfaces should be expected in most cases. A controlled thermal treatment allows for the active control of this cationic disorder and the resulting band alignment (Figure 5d,e).

In conclusion, we have shown that pretreatments in different thermodynamic environments can change the interface properties of high work function metal to metal-oxide heterojunctions due to a varied ionic defect structure and charge screening within the Schottky barrier. The varied transport barrier is linked to the formation of strontium vacancies in the near contact region naturally occurring as a result of Schottky disorder during oxidation.^[29,30,34] At the same time, these defects are responsible for the formation of an insulating surface layer established at the bare surface of Nb:SrTiO₃. We thus emphasize the importance of cationic disorder and defect density for the electrical properties of donor-doped transition metal oxides and their devices. For surfaces and interfaces, cationic disorder can be induced via thermal annealing, while the oxygen pressure during annealing provides a fairly simple control mechanism for the grade of disorder. In this way, localized charges and charge traps can be controlled in functional

devices based on Nb:SrTiO₃ heterointerfaces. Cationic disorder may be actively exploited as a control parameter giving access to band alignment, barrier heights, and electron transport in metal/metal-oxide heterojunctions, as the fundamental driving force for enhanced Schottky disorder in oxidizing conditions can be generalized to most *n*-type oxides.

Experimental Section

0.5 wt% Nb-doped SrTiO₃ single crystals were annealed for 24 h at temperatures of 1050 and 1150 °C in ambient atmosphere (oxidizing conditions) and in 4% H₂/Ar gas flow (reducing conditions). At the end of the annealing procedure the samples were quickly quenched down to room temperature (~30 s) to avoid further changes of the material properties during cooling. Before further treatment we checked the bulk electron concentration of the single crystals by Hall measurements. For all samples, the carrier density matched the Nb-dopant concentration, indicating that no significant defect formation (particularly oxygen vacancy formation) takes place in the bulk of the samples under any applied conditions. 30 nm thick platinum top electrodes with different area sizes were then deposited on the annealed samples by electron beam evaporation through a shadow mask. Electrode sizes were targeted between 200 × 200 μm² and 10 × 10 μm² (Figure 1a). Actual electrode areas were determined by optical microscopy to correct for shadowing effects during metal evaporation.

In order to investigate the junction's contact resistance (R_{sc}) and capacitance (C_{sc}), impedance spectroscopy (Solartron Si 1260, Solartron 1296, 1 Hz < f < 1 MHz) was employed and analyzed using Zview 2 (Ametek scientific instruments). A single semi-circle was modeled by a parallel RC element associated to the Schottky-type interface contact and a series resistance (R_{se}) associated to the lead resistance and Nb:SrTiO₃ bulk contributions (cf. Figure 1b). Additionally, an induction contribution (L_{se}) associated to the leads of the experimental setup was considered.

In order to characterize the rectifying behavior of the Pt/Nb:SrTiO₃ heterojunctions, $I(V)$ -characteristics were measured using a Keithley 2611 source meter. The applied voltage ranged from 0 to +1 V to widely avoid significant resistive switching or electrical breakdown. The Nb:SrTiO₃ backside was grounded, while the potential was applied to the Pt top electrode. A sweep rate of 1 V s⁻¹ was used.

Bare surfaces of the Nb:SrTiO₃ single crystals were further analyzed by in situ conductive-tip atomic force microscopy (C-AFM) with an applied voltage of -0.5 V using a VT-SPM system, Omicron Nanotechnology GmbH. Prior to the experiments the single crystals were annealed *in-situ* in a vacuum chamber at 800 °C in reducing and oxidizing conditions with controlled pressures of 0.1 mbar of oxygen and a base pressure of 10⁻⁸ mbar, respectively. The *in-situ* process avoid surface contamination and thereby increases experimental resolution for the C-AFM imaging.

NAP-XPS was performed in a SpecsTM near ambient pressure XPS instrument using an Al K_α source ($h\nu = 1486.6$ eV) and an emission angle of 90°. In all measurements, the single crystals were electrically contacted from the top using a Ti strip and a Au/Ti top electrode, providing Ohmic electrical contact between sample and analyzer, and avoiding the Schottky barrier discussed in the main paper. All core levels (cf. Supporting Information) and valence band spectra were measured in situ at a temperature of 670 K and an applied oxygen atmosphere ($p(O_2)$) ranging from $\sim 1 \times 10^{-8}$ mbar (UHV) conditions to 5 mbar. In order to determine absolute binding energy values, all spectra were referenced to the Au 4f core level obtained from a Fermi-coupled top electrode.

A theoretical analysis of the heterojunction at the atomic scale was inferred from *ab initio* density functional theory (DFT) simulations combined with the non-equilibrium Green's function (NEGF) formalism. The atomic structure of the Schottky interface was generated, using a supercell dimension of 2 × 2 unit cells in *x*-*y* dimension and a length of 11 unit cells of SrTiO₃ and seven elementary cells of Pt. Three Ti ions were replaced by Nb-dopants to accommodate *n*-type doping of the SrTiO₃ within the supercell. All structures have been relaxed below a

residual force of less than 0.05 eV Å⁻¹. Using the DFT+NEGF formalism as implemented in ATK 2017.12, semi-periodical boundary conditions are applied in perpendicular direction to the Schottky interface. A *k*-point sampling of 3 × 3 × (100) for the electrodes and the periodic directions of the central region was used.^[54,59,60] For the DFT simulation, local basis sets with pseudo-potentials^[61,62] and the Perdew–Burke–Ernzerhof (PBE) exchange potential were applied.^[63] To adjust the bandgap, a Hubbard-*U* of 6 eV was applied to the Sr, Nb, Ti *d*-orbitals and the O *p*-orbitals to fit the bandgap of the isolated SrTiO₃ slab to the experimental value. Further computational details are given in ref. [41].

Supporting Information

Supporting Information is available from the Wiley Online Library or from the author.

Acknowledgements

D.N.M. gratefully acknowledges support by the Juelich Joint Redox Laboratory (JJRL). Furthermore, the authors acknowledge the CERIC-ERIC Consortium for the access to experimental facility and financial support. F.G. acknowledges financial support through DFG1604 (No. 315025796). B.S., F.D., and M.V. would like to thank the Czech Science Foundation for financial support under project no. 17-13427S. The authors gratefully acknowledge the computing time granted for the project no. cjpji70 by the JARA-HPC Vergabegremium on the supercomputer JURECA at the Forschungszentrum Jülich. Details on J.u.I.S. Centre, are given in Journal of large-scale research facilities, 4 (2018). The work was supported by the SFB 917.

Conflict of Interest

The authors declare no conflict of interest.

Keywords

band engineering, defect formation, ionic charge screening, metal/metal-oxide heterojunctions, oxide interfaces

Received: July 31, 2019

Revised: October 16, 2019

Published online: November 18, 2019

- [1] R. Waser, R. Dittmann, G. Staikov, K. Szot, *Adv. Mater.* **2009**, *21*, 2632.
- [2] T. Fujii, M. Kawasaki, A. Sawa, H. Akoh, Y. Kawazoe, Y. Tokura, *Appl. Phys. Lett.* **2005**, *86*, 012107.
- [3] A. Sawa, *Mater. Today* **2008**, *11*, 28.
- [4] C. Baeumer, N. Raab, T. Menke, C. Schmitz, R. Rosezin, P. Müller, M. Andrä, V. Feyer, R. Bruchhaus, F. Gunkel, C. M. Schneider, R. Waser, R. Dittmann, *Nanoscale* **2016**, *8*, 13967.
- [5] E. Mikheev, B. D. Hoskins, D. B. Strukov, S. Stemmer, *Nat. Commun.* **2014**, *5*, 3990.
- [6] H. Y. Hwang, Y. Iwasa, M. Kawasaki, B. Keimer, N. Nagaosa, Y. Tokura, *Nat. Mater.* **2012**, *11*, 103.
- [7] D. G. Schlom, J. Mannhart, *Nat. Mater.* **2011**, *10*, 168.
- [8] R. Hendriks, D. M. Cunha, D. P. Singh, M. Huijben, *ACS Appl. Energy Mater.* **2018**, *1*, 7046.
- [9] H. Kawasoko, S. Shiraki, T. Suzuki, R. Shimizu, T. Hitosugi, *ACS Appl. Mater. Interfaces* **2018**, *10*, 27498.

- [10] D. M. Cunha, T. A. Hendriks, A. Vasileiadis, C. M. Vos, T. Verhallen, D. P. Singh, M. Wagemaker, M. Huijben, *ACS Appl. Energy Mater.* **2019**, *2*, 3410.
- [11] K. Suzuki, K. Kim, S. Taminato, M. Hirayama, R. Kanno, *J. Power Sources* **2013**, *226*, 340.
- [12] M. L. Weber, F. Gunkel, *J. Phys.: Energy* **2019**, *1*, 031001.
- [13] J. D. Baniecki, H. Yamaguchi, C. Harnagea, D. Ricinchi, Z. Gu, J. E. Spanier, T. Yamazaki, H. Aso, *Adv. Energy Mater.* **2019**, *9*, 1803846.
- [14] M. L. Weber, C. Baeumer, D. N. Mueller, L. Jin, C. L. Jia, D. S. Bick, R. Waser, R. Dittmann, I. Valov, F. Gunkel, *Chem. Mater.* **2019**, *31*, 2337.
- [15] A. Sawa, R. Meyer, in *Resistive Switching: From Fundamentals of Nanoionic Redox Processes to Memristive Device Applications* (Ed: D. I. R. Waser), Wiley **2016**.
- [16] D. Cooper, C. Baeumer, N. Bernier, A. Marchewka, C. L. Torre, R. E. Dunin-Borkowski, S. Menzel, R. Waser, R. Dittmann, *Adv. Mater.* **2017**, *29*, 1700212.
- [17] E. Mikheev, J. Hwang, A. P. Kajdos, A. J. Hauser, S. Stemmer, *Sci. Rep.* **2015**, *5*, 11079.
- [18] M. Copel, P. R. Duncombe, D. A. Neumayer, T. M. Shaw, R. M. Tromp, *Appl. Phys. Lett.* **1997**, *70*, 3227.
- [19] R. Schafranek, S. Payan, M. Maglione, A. Klein, *Phys. Rev. B* **2008**, *77*, 195310.
- [20] A. Ohtomo, H. Y. Hwang, *Appl. Phys. Lett.* **2004**, *84*, 1716.
- [21] E. M. Bourim, D. W. Kim, *Curr. Appl. Phys.* **2013**, *13*, 505.
- [22] Y. Hikita, K. Nishio, L. C. Seitz, P. Chakthranont, T. Tachikawa, T. F. Jaramillo, H. Y. Hwang, *Adv. Energy Mater.* **2016**, *6*, 1502154.
- [23] K. J. May, D. P. Fenning, T. Ming, W. T. Hong, D. Lee, K. A. Stoerzinger, M. D. Biegalski, A. M. Kolpak, Y. Shao-Horn, *J. Phys. Chem. Lett.* **2015**, *6*, 977.
- [24] S. A. Chambers, Y. Du, R. B. Comes, S. R. Spurgeon, P. V. Sushko, *Appl. Phys. Lett.* **2017**, *110*, 082104.
- [25] L. Kornblum, M. D. Morales-Acosta, E. N. Jin, C. H. Ahn, F. J. Walker, *Adv. Mater. Interfaces* **2015**, *2*, 1500193.
- [26] F. Gunkel, R. Waser, A. H. H. Ramadan, R. A. De Souza, S. Hoffmann-Eifert, R. Dittmann, *Phys. Rev. B* **2016**, *93*, 245431.
- [27] A. Marchewka, D. Cooper, C. Lenser, S. Menzel, H. Du, R. Dittmann, R. E. Dunin-Borkowski, R. Waser, *Sci. Rep.* **2015**, *4*, 6975.
- [28] D. Kan, Y. Shimakawa, *Appl. Phys. Lett.* **2013**, *103*, 142910.
- [29] M. Andrä, F. Dvorák, M. Vorokhta, S. Nemšák, V. Matolín, C. M. Schneider, R. Dittmann, F. Gunkel, D. N. Mueller, R. Waser, *APL Mater.* **2017**, *5*, 056106.
- [30] M. Andrä, H. Bluhm, C. M. Schneider, R. Dittmann, R. Waser, D. N. Mueller, F. Gunkel, *Phys. Rev. Mater.* **2019**, *3*, 044604.
- [31] C. Baeumer, C. Schmitz, A. Marchewka, D. N. Mueller, R. Valenta, J. Hackl, N. Raab, S. P. Rogers, M. I. Khan, S. Nemsak, M. Shim, S. Menzel, C. M. Schneider, R. Waser, R. Dittmann, *Nat. Commun.* **2016**, *7*, 12398.
- [32] T. Fujii, M. Kawasaki, A. Sawa, Y. Kawazoe, H. Akoh, Y. Tokura, *Phys. Rev. B* **2007**, *75*, 165101.
- [33] R. Moos, K. H. Hardtl, *J. Am. Ceram. Soc.* **1997**, *80*, 2549.
- [34] R. Meyer, A. F. Zurhelle, R. A. De Souza, R. Waser, F. Gunkel, *Phys. Rev. B* **2016**, *94*, 115408.
- [35] J. Daniels, K. H. Hardtl, D. Hennings, R. Wernicke, *Phillips Research Reports* **1976**, *31*, 505.
- [36] D. M. Smyth, *The Defect Chemistry of Metal Oxides*, Oxford University Press, Oxford **2000**.
- [37] F. Gunkel, P. Brinks, S. Hoffmann-Eifert, R. Dittmann, M. Huijben, J. E. Kleibeuker, G. Koster, G. Rijnders, R. Waser, *Appl. Phys. Lett.* **2012**, *100*, 052103.
- [38] C. Rodenbücher, M. Luysberg, A. Schwedt, V. Havel, F. Gunkel, J. Mayer, R. Waser, *Sci. Rep.* **2016**, *6*, 32250.
- [39] R. A. van der Berg, P. W. M. Blom, J. F. M. Cillessen, R. M. Wolf, *Appl. Phys. Lett.* **1995**, *66*, 697.
- [40] R. Neville, B. Hoeneisen, C. Mead, *J. Appl. Phys.* **1972**, *43*, 2124.
- [41] C. Funck, A. Marchewka, C. Bäumer, P. C. Schmidt, P. Müller, R. Dittmann, M. Martin, R. Waser, S. Menzel, *Adv. Electron. Mater.* **2018**, *4*, 1800062.
- [42] C. Funck, S. Menzel, *AIP Adv.* **2019**, *9*, 045116.
- [43] M. Lewin, C. Baeumer, F. Gunkel, A. Schwedt, F. Gaussmann, J. Wueppen, P. Meuffels, B. Jungbluth, J. Mayer, R. Dittmann, R. Waser, T. Taubner, *Adv. Funct. Mater.* **2018**, *28*, 1802834.
- [44] O. N. Tufte, P. W. Chapman, *Phys. Rev.* **1967**, *155*, 796.
- [45] A. Spinelli, M. A. Torija, C. Liu, C. Jan, C. Leighton, *Phys. Rev. B* **2010**, *81*, 155110/1–14.
- [46] R. A. D. Souza, *Phys. Chem. Chem. Phys.* **2009**, *11*, 9939.
- [47] R. A. De Souza, F. Gunkel, S. Hoffmann-Eifert, R. Dittmann, *Phys. Rev. B* **2014**, *89*, 241401.
- [48] L. Dudy, M. Sing, P. Scheiderer, J. D. Denlinger, P. Schütz, J. Gabel, M. Buchwald, C. Schlueter, T. L. Lee, R. Claessen, *Adv. Mater.* **2016**, *28*, 7443.
- [49] Z. Wang, S. M. Walker, A. Tamai, Y. Wang, Z. Ristic, F. Y. Bruno, A. de la Torre, S. Ricco, N. C. Plumb, M. Shi, P. Hlawenka, J. Sanchez-Barriga, A. Varykhalov, T. K. Kim, M. Hoesch, P. D. C. King, W. Meevasana, U. Diebold, J. Mesot, B. Moritz, T. P. Devereaux, M. Radovic, F. Baumberger, *Nat. Mater.* **2016**, *15*, 835.
- [50] A. F. Santander-Syro, O. Copie, T. Kondo, F. Fortuna, S. Pailhes, R. Weht, X. G. Qiu, F. Bertran, A. Nicolaou, A. Taleb-Ibrahimi, P. L. Fevre, G. Herranz, M. Bibes, N. Reyren, Y. Apertet, P. Lecoeur, A. Barthelemy, M. J. Rozenberg, *Nature* **2011**, *469*, 189.
- [51] Y. Chen, W. Jung, Z. Cai, J. J. Kim, H. L. Tuller, B. Yildiz, *Energy Environ. Sci.* **2012**, *5*, 7979.
- [52] R. Bachelet, F. Sánchez, F. J. Palomares, C. Ocal, J. Fontcuberta, *Appl. Phys. Lett.* **2009**, *95*, 141915.
- [53] S. A. Chambers, Y. Du, Z. Zhu, J. Wang, M. J. Wahila, L. F. J. Piper, A. Prakash, J. Yue, B. Jalan, S. R. Spurgeon, D. M. Kepaptsoglou, Q. M. Ramasse, P. V. Sushko, *Phys. Rev. B* **2018**, *97*, 245204.
- [54] D. Stradi, U. Martinez, A. Blom, M. Brandbyge, K. Stokbro, *Phys. Rev. B* **2016**, *93*, 155302/1.
- [55] W. Wang, T. Lee, M. A. Reed, *Phys. Rev. B* **2003**, *68*, 035416.
- [56] T. Tachikawa, M. Minohara, Y. Hikita, C. Bell, H. Y. Hwang, *Adv. Mater.* **2015**, *27*, 7458.
- [57] E. Mikheev, J. Hwang, A. P. Kajdos, A. J. Hauser, S. Stemmer, *Sci. Rep.* **2015**, *5*, 11079.
- [58] A. Marchewka, B. Roesgen, K. Skaja, H. Du, C. L. Jia, J. Mayer, V. Rana, R. Waser, S. Menzel, *Adv. Electron. Mater.* **2016**, *2*, 1500233/1–13.
- [59] M. Brandbyge, J. Mozos, P. Ordejon, J. Taylor, K. Stokbro, *Phys. Rev. B* **2002**, *65*, 165401/1–17.
- [60] J. Soler, E. Artacho, J. Gale, A. Garcia, J. Junquera, P. Ordejon, D. Sanchez-Portal, *J. Phys. Condens. Mat.* **2002**, *14*, 2745.
- [61] N. Troullier, J. Martins, *Phys. Rev. B: Condens. Matter* **1991**, *43*, 1993.
- [62] D. Hamann, *Phys. Rev. B* **1989**, *40*, 2980.
- [63] J. P. Perdew, K. Burke, M. Ernzerhof, *Phys. Rev. Lett.* **1996**, *77*, 3865.